Conference on Modelling Fluid Flow (CMFF'18)
The 17th International Conference on Fluid Flow Technologies
Budapest, Hungary, September 4-7, 2018

MAP-BASED MODELLING OF HIGH-RAYLEIGH-NUMBER TURBULENT CONVECTION IN PLANAR AND SPHERICAL CONFINEMENTS

Marten KLEIN[1], Heiko SCHMIDT[2], David O. LIGNELL[3]

[1] Corresponding Author. Department of Numerical Fluid and Gas Dynamics, Faculty of Mechanical Engineering, Electrical and Energy Systems, Brandenburg University of Technology (BTU) Cottbus-Senftenberg. Siemens-Halske-Ring 14, D-03046 Cottbus, Germany. Tel.: +49 355 695 127, Fax: +49 355 694 891, E-mail: marten.klein@b-tu.de
[2] Department of Numerical Fluid and Gas Dynamics, Faculty of Mechanical Engineering, Electrical and Energy Systems, Brandenburg University of Technology (BTU) Cottbus-Senftenberg. E-mail: heiko.schmidt@b-tu.de
[3] Department of Chemical Engineering, Brigham Young University. E-mail: davidlignell@byu.edu

ABSTRACT

High-Rayleigh-number (high-Ra) turbulent convection is numerically studied in planar and spherical confinement geometries using the one-dimensional turbulence (ODT) model. Stochastic mapping events are used in ODT to model turbulent advection along a representative line of the turbulent flow. The ODT implementation used is fully adaptive and based on a finite volume discretisation in the Lagrangian frame of reference. Model parameters are first optimised for an air-filled (Prandtl number $Pr = 0.7$) planar confinement at $Ra = 3 \times 10^{10}$. After that, convection is studied in spherical geometry for various radius ratios, gravity profiles, and Rayleigh numbers by keeping $Pr = 1$ and the model parameters fixed. The simulated thermal and viscous boundary layers exhibit good agreement with reference data up to wide gap widths even for relatively low Rayleigh numbers. Present results suggests that ODT is mainly applicable for $Ra \gtrsim 10^7$ (with $Pr \simeq 1$). The model formulation is robust and yields reasonable results for a broad range of physical control parameters.

Keywords: boundary layers, geophysical flows, one-dimensional turbulence, Rayleigh–Bénard convection, turbulence modelling

NOMENCLATURE

$A,\ B$	$[-]$	thermal log layer slope, offset
C	$[-]$	eddy-rate parameter
E	$[J]$	energy
$J,\ K$	$[m]$	kernel functions
L	$[m]$	gap width
Nu	$[-]$	Nusselt number
Pr	$[-]$	Prandtl number
R	$[m]$	radius
Ra	$[-]$	Rayleigh number
T	$[K]$	temperature
U	$[m/s]$	horizontal velocity
V	$[m^3]$	eddy volume
Z	$[-]$	viscous-penalty parameter
$b,\ c$	$[1/s]$	kernel coeff.
g	$[m/s^2]$	gravity
l	$[m]$	eddy size
$r,\ x,\ z$	$[m]$	radial, 1-D, vertical coord.
t	$[s]$	time
u	$[m/s]$	velocity
$\underline{e}$	$[-]$	unit vector
α	$[-]$	isotropy parameter
β	$[1/K]$	thermal expansion coeff.
δ	$[m]$	boundary layer thickness
η	$[-]$	radius ratio
γ	$[-]$	distribution parameter
κ	$[m^2/s]$	thermal diffusivity
ν	$[m^2/s]$	kinematic viscosity
ρ	$[kg/m^3]$	density
σ	$[-]$	standard deviation
τ	$[s]$	eddy timescale
$\mathcal{E}$	$[-]$	eddy event
Θ	$[-]$	dimensionless temperature

Subscripts and Superscripts

T	temperature-related
U	velocity-related
b	bulk
cw, hw	cool, hot wall
f	free-fall
i	inner
kin	kinetic
max	maximum value
opt	optimal value
o	outer
pot	potential
ref, 0	reference value
vp	viscous penalty
$i,\ j$	coordinate index
$'$	triplet-mapped
$-$	temporal mean

1. INTRODUCTION

Turbulent convection denotes the chaotic flow driven by buoyancy forces due to an unstable temperature stratification. The developing flow itself influences the temperature distribution which results in a complex interplay between the momentum and temperature fields. A quantitative understanding of turbulent convection is relevant for many applications where the heat transport is of concern. These are typically technological (like cooling systems) or geophysical problems (like atmospheric or mantle convection; see e.g. [1] and references therein).

A model problem for such flows is Rayleigh–Bénard (RB) convection. The classical RB setup is a fluid-filled cylinder with a heated bottom and cooled top as shown in Figure 1(a). For geophysical applications, the spherical confinement geometry is sometimes important (e.g. in mantle convection) so that a spherical shell configuration seems more appropriate. This case is shown in Fig. 1(b) where fluid is confined between an inner hot and an outer cold sphere. The background gravity acts in radial direction and its strength $g(r)$ can vary with the radius r due to the internal mass distribution (e.g. [2]). The spherical confinement geometry is addressed by the radius ratio $\eta = r_\mathrm{i}/r_\mathrm{o}$, which replaces the aspect ratio $2R/L$ used in the planar case.

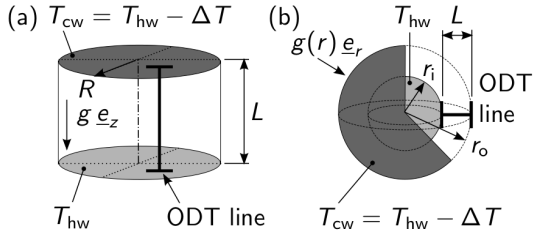

Figure 1. Schematic showing a planar (a) and a spherical Rayleigh–Bénard setup (b).

Turbulent convection in a selected geometry is characterised by the Rayleigh and the Prandtl number, which are given by

$$Ra = \frac{g_0 \beta \Delta T L^3}{\nu \kappa} \quad \text{and} \quad Pr = \frac{\nu}{\kappa}, \tag{1}$$

where g_0 is the reference gravity, $\Delta T = T_\mathrm{hw} - T_\mathrm{cw}$ is the imposed temperature difference between the hot and cold wall, and L is the distance between those walls, respectively, β is the thermal expansion coefficient, ν the kinematic viscosity, and κ the thermal diffusivity of the working fluid. Practically relevant values of the Rayleigh number encompass several orders of magnitude ($10^6 \lesssim Ra \lesssim 10^{27}$ [1]). The Prandtl number is, by contrast, close to one for many gases and liquids. Therefore, the present paper focuses on the feasibility of high-Ra numerical simulations of turbulent convection with $Pr \simeq 1$.

Direct numerical simulations (DNSs) have reached $Ra = 2 \times 10^{12}$ in three dimensions (3-D) [3] and $Ra = 10^{14}$ in 2-D [4] for $Pr = O(1)$. Such simulations are extremely costly and in the case of long-time simulations and/or large aspect ratios practically limited by $10^9 \lesssim Ra \lesssim 10^{10}$ [1, 2, 5, 6].

Accurate and efficient modelling strategies are needed if one wishes to increase the accessible Rayleigh number range within the considerable future. The difficulty is that gradient-diffusion approaches do not allow for scale interactions that can be crucial for the flow evolution and the accuracy of the predicted heat transfer. A fundamentally different modelling approach is therefore used here: the so-called one-dimensional turbulence (ODT) model [7, 8, 9, 10]. ODT is a stochastic turbulence model that aims to resolve all scales of the turbulent flow. This is made feasible by dimensional model reduction.

The rest of this paper is organised as follows. Section 2 addresses relevant aspects of the ODT model. In Section 3, ODT results for a planar (cylindrical) RB cell are shown and the selection of model parameters is discussed. In Section 4, ODT results for spherical geometries are shown for various radius ratios, gravity profiles, and Rayleigh numbers keeping the Prandtl number and the model parameters fixed. Section 5 closes with some concluding remarks.

2. ODT MODEL FORMULATION

Numerical simulations of convecting flows are performed with the temporal ODT formulation [7, 8, 10]. The computational domain is a statistically representative line of the turbulent flow along which velocity and temperature profiles are evolved in time. The ODT line (the thick 'H'-like lines in Fig. 1) forms a 1-D computational domain, which is approximately viewed as a closed system. The line is oriented in vertical (radial) direction in planar (spherical) geometry so that the molecular and map-based transport is performed in the direction of the largest mean gradients.

2.1. Governing equations

The governing equations are the conservation of mass, momentum, and energy plus an equation of state. Here the Oberbeck–Boussinesq approximation $\rho(T) = \rho_0 \left[1 - \beta (T - T_0)\right]$ is used which implies weak density fluctuations $|\rho(T) - \rho_0| \ll \rho_0$. The density is therefore treated as constant except for the buoyancy forces. The ODT equations read (planar; see [10])

$$\frac{\partial u_i}{\partial t} + \mathcal{E}_i(u_j, T) = \nu \frac{\partial^2 u_i}{\partial z^2}, \tag{2}$$

$$\frac{\partial T}{\partial t} + \mathcal{E}_T(u_j, T) = \kappa \frac{\partial^2 T}{\partial z^2}. \tag{3}$$

These Eqs. are closed with isothermal no-slip boundary conditions at the walls.

Molecular diffusion is resolved in 1-D (along the ODT line) but this deterministic evolution is interrupted by stochastic mapping events (eddy events) $\mathcal{E}$

which mimic the effect of turbulent stirring. Both $\mathcal{E}_i$ and $\mathcal{E}_T$ obtain their physical units (i.e. as a rate of change of the velocity or the temperature, respectively) from (i) the map-induced fluctuation of the property under consideration and (ii) an inverse eddy timescale τ^{-1} (see Eq. (6) below). The buoyancy and fluctuating pressure gradient forces are modelled within the stochastic term $\mathcal{E}_i$, whereas $\mathcal{E}_T$ is simply advecting the temperature scalar. The forces in $\mathcal{E}_i$ depend on the current state of the (1-D) temperature and velocity fields in analogy to the (3-D) flow in reality.

In spherical geometry, one has to take into account that the transport along the ODT line is in radial direction. It has been suggested to view the ODT line as a solid angle element with infinitesimal extent in the two off-line directions [11]. The second derivatives $\partial_z^2(\cdot)$ in Eqs. (2) and (3) therefore have to be replaced with $r^{-2}\partial_r[r^2\partial_r(\cdot)]$. The mapping inside the stochastic terms is also affected but will be addressed below.

2.2. Discretisation strategy

Eqs. (2) and (3) are discretised with finite volumes on an adaptive grid in the Lagrangian frame of reference [11, 12]. Here, the smallest allowed cell size and the resolution of the fixed statistics grid are both about 30 times smaller than the expected thermal boundary layer thickness (e.g. [1, 2, 3, 5]), whereas the largest allowed cell size was set to a low percentage of the domain size. It was checked that the simulated flow statistics are independent of the selected bounds for the grid cell sizes.

A low-order explicit time integration scheme was used in this study since the stochastic mapping events destroy higher-order accuracy in time and since $Pr \simeq 1$ yields comparable spatio-temporal scales in the velocity and the temperature. The time step is also adaptive but constrained by the sampling of eddy events (see below) and the critical Courant number of the scheme.

2.3. Eddy events

Eddy events are the fundamental building block of ODT. Each eddy consists of a permutation of fluid parcels along a randomly selected line interval. This permutation is more generally described by a measure-preserving map, which yields conservation of mass, momentum, and energy in an integral sense. For physical soundness it is required that a mapped property profile features locally increased gradients but is otherwise continuous. These requirements are addressed by the triplet map (TM) [7].

The TM consists of (i) the compression of a property profile to a third of its original length, (ii) pasting of two copies of the compressed profiles to fill the eddy interval, and (iii) a flip of the central copy to ensure continuity. This algorithm is used in the adaptive ODT implementation [11, 12] to increase the resolution where the flow is turbulent.

Figure 2 shows the TM for an initially linear profile. The number of grid points (+) has tripled across the eddy interval. In spherical geometry, the TM has to be adjusted to maintain the conservation properties. The crucial point lies in the radial integration over $r^2\,\mathrm{d}r$ instead of $l^2\,\mathrm{d}z$ in the case of planar geometry. This has to be compensated by geometric stretching of individual grid cell positions in the map image. Here, the so-called TMA has been used [11]. TMA is characterised by a uniform partition of the fluid volume among the three map images (every image carries 1/3 of the total eddy volume). An example of the TMA is shown in Fig. 2 which shows the geometric stretching effect.

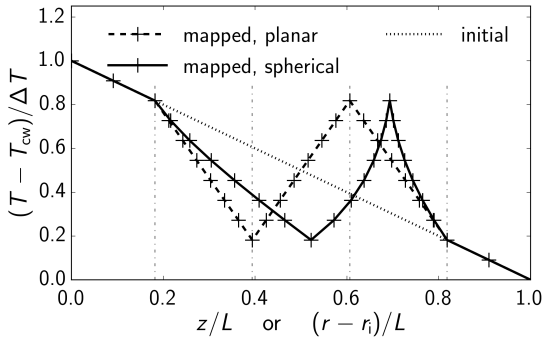

Figure 2. Visualisation of the triplet map in axial and radial directions, denoted planar and spherical, respectively. The triplet map in spherical geometry is TMA [11].

The energetic consequences of a TM application need to be considered to ensure physical soundness of the model. The present formulation uses three velocity components (so-called 'vector ODT'). This yields the following effects on the temperature T and velocity profiles u_i [8, 11, 12]:

$$\mathcal{E}_T: \qquad T(x) \to T'(x), \tag{4}$$

$$\mathcal{E}_i: \qquad u_i(x) \to u_i'(x) + c_i K(x) + b_i J(x). \tag{5}$$

Here, x is the ODT line coordinate, which is either vertical (planar case) or radial (spherical case). The prime indicates application of the triplet map. $K(x)$ and $J(x) = |K(x)|$ are kernel functions defined by the triplet map [7, 9, 11]. The coefficients c_i and b_i are obtained by enforcing conservation properties together with a maximisation of the energy exchange between the velocity components for the ODT isotropy parameter $0 < \alpha \leq 1$. This mechanism is omitted in single-velocity ODT due to $\alpha = 0$. By contrast, the change of the potential energy is always included in c_i and b_i but depends on the parameters γ_i, which model the distribution of the potential energy release to (or the take-up from) the velocity components and need to sum up to one.

2.4. Eddy selection

Eddy events are characterised by three random variables: eddy size, position, and time of occurrence. These can be sampled in principle from

the eddy-rate distribution λ, where $\lambda(l, x_0, t)\,\mathrm{d}l\,\mathrm{d}x_0\,\mathrm{d}t$ gives the number of eddies in the size range $[l, l + \mathrm{d}l]$ and the position range $[x_0, x_0 + \mathrm{d}x_0]$ during the time interval $[t, t + \mathrm{d}t]$. (In planar (spherical) geometry the eddy position x_0 has to be replaced by z_0 (r_0).) However, the eddy-rate distribution depends on the current state of the flow and is thus unknown.

To avoid a repeated and costly construction of λ, an alternative, more cost-efficient thinning-and-rejection method is used in practice for the selection of eddies [7]. The eddy-rate distribution can be written as $\lambda = C\,\tau^{-1}\,l^{-2}$ in terms of the eddy timescale τ and the eddy length scale l. C is the eddy-rate parameter, which is related to the turbulence intensity. The eddy timescale τ depends on the extractable eddy energy and is for a Boussinesq fluid given by

$$\frac{1}{\tau} = \sqrt{\frac{2}{\rho_0 l^2 V(l)}\Big(E_{\mathrm{kin}} + E_{\mathrm{pot}} - Z E_{\mathrm{vp}}\Big)}. \qquad (6)$$

E_{kin}, E_{pot}, and E_{vp} denote the kinetic, potential, and viscous penalty energy, respectively, and $V(l)$ is the eddy volume [11]. The kinetic energy E_{kin} is given by the extractable energy due to TM application. In vector ODT, E_{kin} is computed by summing all three square kernel-weighted velocity components [8]. The viscous penalty E_{vp} is proportional to ν^2/l^2 and effectively defines a cut-off length scale (i.e. the Kolmogorov scale) [8]. The viscous penalty parameter Z can be used to adjust the range of scales represented in the ODT model.

Wunsch and Kerstein [10] formulated the ODT eddy energetics for convecting flows with a single representative velocity scalar. A novelty of the present formulation is the extension of the potential energy treatment to spherical geometry [11] and vector ODT [8, 9]. E_{pot} is obtained by computing the total lifting work due to the rearrangement of fluid parcels under the TM. This energy is either released to ($E_{\mathrm{pot}} > 0$) or taken from ($E_{\mathrm{pot}} < 0$) the flow. For a Boussinesq fluid in spherical geometry and subject to position-dependent gravity (here $g(r) < 0$) one has

$$E_{\mathrm{pot}} = -\rho_0 \beta \int_{r_0}^{r_0+l} G(r)\,\left[T'(r) - T(r)\right]\,r^2 \mathrm{d}r \qquad (7)$$

$$\text{with} \qquad G(r) = \int_0^r g(x)\,\mathrm{d}x. \qquad (8)$$

Switching back to planar geometry is easily done by replacing r with z and $r^2\,\mathrm{d}r$ with $l^2\,\mathrm{d}z$, but the line integral over $\mathrm{d}x$ remains unchanged. In both cases, only candidate eddies with positive net extractable energy are physically plausible and only these are considered for implementation.

It remains to determine the model parameters C and Z for a given flow configuration with the aid of reference data. This is done below for turbulent convection in a planar RB cell before moving on to spherical geometry.

3. PLANAR GEOMETRY

The ODT model is now applied to RB convection in planar confinement geometry with uniform gravity ($g = -g_0 < 0$ in accord with Fig. 1(a)). Two different ODT setups are considered. One is single-velocity ODT (in analogy to [10]) where the kinetic energy is contained entirely in a representative velocity scalar. This case is realised in vector ODT by selecting $\alpha = 0$ and $(\gamma_i) = (1, 0, 0)$. The other setup is vector ODT with a tendency to small-scale isotropy and uniform release (and take-up) of potential energy to (from) the velocity components. This case is realised with $\alpha = 2/3$ and $(\gamma_i) = (1/3, 1/3, 1/3)$. The default values are set to $C = 60$ and $Z = 220$ which will be discussed below.

3.1. Bulk flow

Figure 3 shows ODT results for turbulent convection in a planar RB cell at $Ra = 3 \times 10^{10}$ and $Pr = 0.7$ (air). The reference temperature, velocity, and time scales are given by the imposed temperature difference, the free-fall velocity $U_{\mathrm{f}} = \sqrt{g_0 \beta\,\Delta T\,L}$, and the free-fall time $t_{\mathrm{f}} = L/U_{\mathrm{f}}$, respectively.

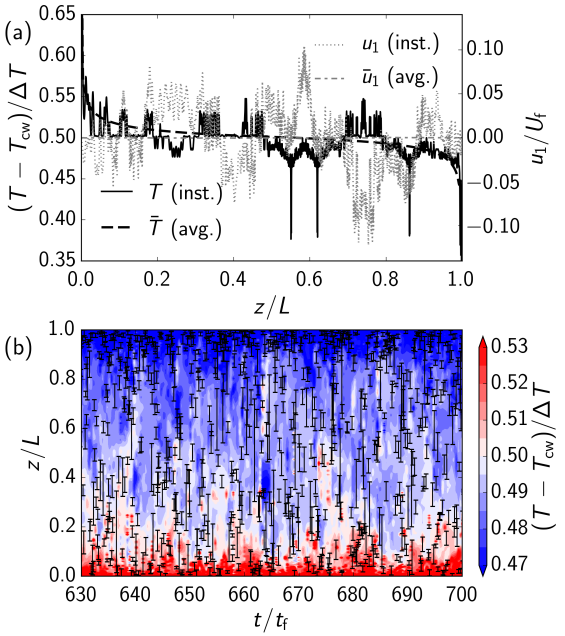

Figure 3. Vertical profiles of the temperature and one horizontal velocity component (a). Hovmöller diagram of the bulk temperature with superimposed eddy events (b, colour online).

The vertical profiles shown in Fig. 3(a) have been obtained with the vector formulation, whereas the temperature distribution in Fig. 3(b) has been obtained with single-velocity ODT. Eddy events are also shown in Fig. 3(b) by lines (only every 10th eddy is given due to visibility reasons). Both panels exhibit a broad range of scales in the instantaneous fields revealing steep temperature and velocity gradients in the whole domain. The mean temperature

shown in Fig. 3(a) exhibits strong gradients only near the walls, but it is almost constant in the bulk of fluid. This bulk temperature is the average of the prescribed wall temperatures implying symmetric boundary layers discussed further in the next section.

3.2. Thermal and viscous boundary layer

ODT results are evaluated with respect to the thermal and viscous boundary layers using the two model setups mentioned above. The flow statistics are symmetric to the mid plane $z = L/2$ (Fig. 3(a)) so that it is sufficient to consider the boundary layers over the heated bottom wall.

Figure 4 shows profiles of low-order statistical quantities for the thermal and the viscous boundary layer. ODT results are shown together with reference DNS data for $Ra = 3 \times 10^{10}$ for a cylindrical RB cell with aspect ratio one [5]. This reference provides results for the thermal and the viscous boundary layer along the axis of the RB cell. Another reference data set was obtained at somewhat smaller $Ra = 2 \times 10^{10}$ and aspect ratio 1/2 [3].

Profiles of the dimensionless mean temperature are shown in Fig. 4(a). This temperature is given by

$$\Theta(z/L) = \frac{\bar{T}(z/L) - T_\mathrm{b}}{\Delta T}, \tag{9}$$

where $T_\mathrm{b} = (T_\mathrm{hw} + T_\mathrm{cw})/2$ only for a Boussinesq fluid in planar geometry with uniform gravity. One can see that all ODT setups and the two reference data sets yield virtually the same temperature gradient at the wall. This implies that all configurations exhibit the same local heat transfer (Nusselt number). The near-wall temperature gradient is visualised by a linear extrapolation, which is shown as dash-dotted line that appears curved in the semi-logarithmic axes.

Further away from the wall, the mean temperature exhibits a logarithmic region [3] (thin dashed lines in Fig. 4(a)). This is captured by ODT, in particular for the model parameters $C = 60$, $Z = 220$. The fits shown have been obtained for the interval $10^{-2} \le z/L \le 10^{-1}$ assuming

$$\Theta(z/L) = A \, \ln(z/L) + B. \tag{10}$$

Figs. 4(b) and (c) show normalised wall-normal profiles of the standard deviation of the temperature (σ_T) and the horizontal velocity (σ_U) fluctuations, respectively. These standard deviations are given by

$$\sigma_T = \sqrt{\overline{T^2 - \bar{T}^2}} \quad \text{and} \quad \sigma_U = \sqrt{\overline{u_1^2 + u_2^2}}. \tag{11}$$

One can see in Fig. 4 that the profile of σ_T is quite well captured near the wall and towards the bulk, but it also experiences a local minimum, which is absent in the reference DNS [5]. A similar, but less severe structure is also exhibited by σ_U. These local fluctuation minima are a known modelling error of ODT related to the self-similarity of the triplet map [12]. The modelling error remains localised in the mixing layer at small but finite distance from the wall. This is very similar in forced convection [13].

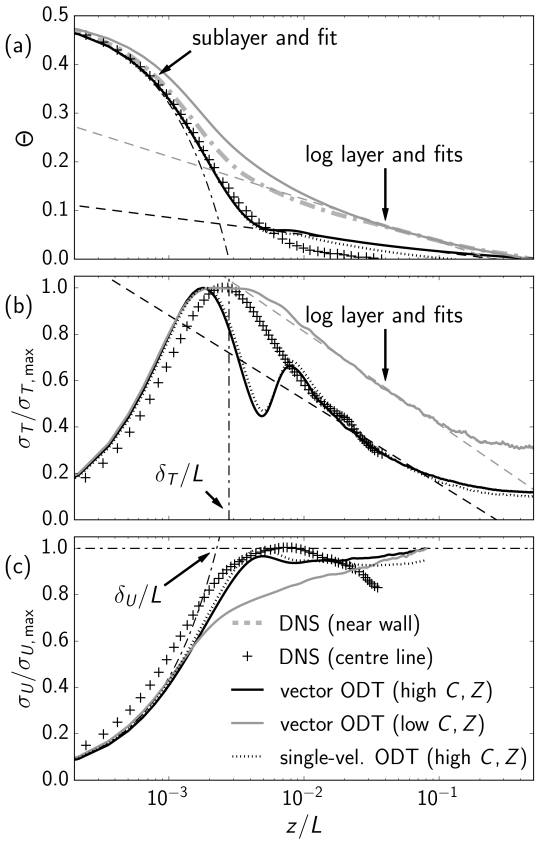

Figure 4. Boundary layer profiles over the heated wall showing the mean temperature (a) and the standard deviations of the temperature (b) and the horizontal velocity fluctuations (c), respectively. Three ODT setups are compared with reference data from [3] (− · −) and [5] (+), respectively.

Also shown in Fig. 4 are ODT results for an alternative set of model parameters ($C = 12$, $Z = 9$; solid grey line). These parameters yield substantially more small-scale mixing. The flow statistics differ notably from those obtained with the other set of parameters, especially with increasing distance from the wall. Two points are worth to be noted. One is that smaller values of C and Z yield mean temperature profiles that are more representative for the vertical boundary layer flow near the outer wall of a cylindrical RB cell [3]. Another is the absence of the local fluctuation minima which suggests that the imprint of the triplet map is only notable near the wall when the scale range is sufficiently truncated. This truncation is used in ODT to improve the fluctuation statistics thus mimicking presence of 3-D vortical structures (like plumes), which are not resolved directly in ODT.

Altogether, ODT statistics of RB convection in planar geometry are representative for a cylindrical cell. However, ODT does *not* reproduce the centreline statistics. This is likely due to the unresolved small-scale structures (plumes) and large-scale circulation (LSC, e.g. [1, 5]).

3.3. Selection of model parameters

The ODT model parameters need be selected such that the flow statistics are reasonably well reproduced for a given flow configuration. The aim is to find a set of model parameters, which minimises the error in relevant statistical quantities while maintaining computational efficiency. These parameters should also yield reasonable results for a large range of physical control parameters (as e.g. in [10, 13]).

Here, high-Ra turbulent convection in planar geometry with $2 \times 10^{10} \leq Ra \leq 3 \times 10^{10}$ and $Pr = 0.7$ has been selected as test case. Various statistical quantities are available from measurements and DNSs (e.g. [1, 3, 5]). Some of these quantities are sensible to the near-wall flow (like the Nusselt number or the boundary layer thickness) and others to the flow further away from the wall (like the logarithmic region or the bulk temperature). All the quantities mentioned were investigated.

Figure 5 gives an overview of the simulations conducted for various C and Z. Each marker represents a single simulation continued until the mean and fluctuation statistics were converged. The markers vary in contrast and size to visualise the deviations in the logarithmic region (by means of the slope A in Eq. (10)) and the Nusselt number, respectively. Latter is computed here via the mean temperature gradient at the heated or cooled wall,

$$Nu = \left| (\mathrm{d}\bar{T}/\mathrm{d}z)_{\mathrm{cw/hw}} \right| \Big/ (\Delta T/L)\,. \tag{12}$$

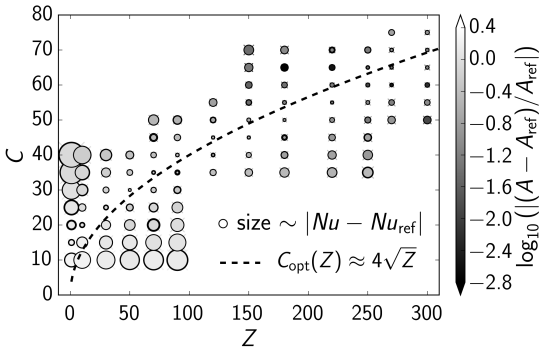

Figure 5. Relative error as function of the model parameters C and Z for vector ODT in comparison to reference data [1, 3, 5] using the Nusselt number Nu (marker size) and the thermal log layer slope A (shading) as indicator. Single-velocity ODT gives similar results.

It is interesting that the optimal C and Z with the smallest deviations in Nu and A fall approximately on the curve $C_{\mathrm{opt}}(Z) \approx 4\sqrt{Z}$. This is similar to a previous study of Wunsch and Kerstein [10].

The ODT results are further evaluated by using additional criteria like the thermal log layer offset B in Eq. (10) or the thermal δ_T and viscous boundary layer thickness δ_U. Both thicknesses have been computed with the slope method (see annotations in Fig. 4). Details are given in Table 1, where values in brackets give the error margin (±) for the last digit.

Table 1. Statistical quantities for $Ra = 3 \times 10^{10}$, $Pr = 0.7$ and $C = 60$, $Z = 220$: From the top, the rows contain the reference value (margin), the single-velocity, and the vector ODT result.

Nu	δ_T/L	δ_U/L	$-A$	$-B$
176(5)	0.0030(3)	0.0027(3)	0.010(5)	0.020(5)
173	0.00288	0.00251	0.0143	0.0154
180	0.00277	0.00253	0.0143	0.0205

4. SPHERICAL GEOMETRY

This section presents ODT results for thermal convection in spherically confined geometry (see Fig. 1(b)). The Prandtl number is fixed at $Pr = 1$, but the Rayleigh number, the radius ratio, and the gravity are varied. To reduce the complexity, only single-velocity ODT is considered here selecting $C = 60$, $Z = 220$ (optimal parameters in planar geometry).

The gravity profile $g(r)$ results from the mass distribution in the spherical configuration. It is considered to remain unaffected by the convecting flow. The following gravity profiles are of practical relevance (e.g. [2]): $g/g_0 \in \{r/r_{\mathrm{o}}, 1, (r_{\mathrm{o}}/r)^2, (r_{\mathrm{o}}/r)^5\}$, where g_0 is the reference gravity at the outer radius.

In contrast to the planar setup, one is now facing a geometry parameter in ODT. This is the radius ratio $0 < \eta = r_{\mathrm{i}}/r_{\mathrm{o}} \leq 1$. Small values correspond to wide-gap configurations, whereas $\eta \to 1$ yields the limiting case of an infinite planar domain.

4.1. Variation of radius ratio and gravity

The dependencies of thermal convection on the radius ratio and the background gravity are investigated by comparing ODT with reference DNS results. The Rayleigh number is varied across the range $7 \times 10^5 \leq Ra \leq 10^7$ in accord with the reference data [2] to keep $Nu \sim 10$ constant.

Figure 6 shows radial profiles of the mean temperature for various radius ratios in the case of $g(r) \propto r^{-2}$. This gravity profile compensates exactly the geometric stretching along the radius and is therefore of fundamental interest [2]. One can see in Fig. 6 that the bulk temperature and boundary layers are notably affected by the radius ratio. This dependency is quite well captured by ODT even though the Rayleigh number is much smaller than 10^{10} for which the optimal model parameters have been obtained in planar geometry. One can therefore expect a decrease of the modelling error with increasing Ra and $\eta \to 1$. Latter is indeed observed for the bulk temperature.

Figure 7 shows radial profiles of the mean temperature for various gravity profiles in the case of a wide gap ($\eta = 0.6$). A larger bulk temperatures is obtained for a smaller exponent in the background gravity profile when Nu is approximately constant. Interestingly, the modelling error is smallest for $g(r) \propto r^{-5}$

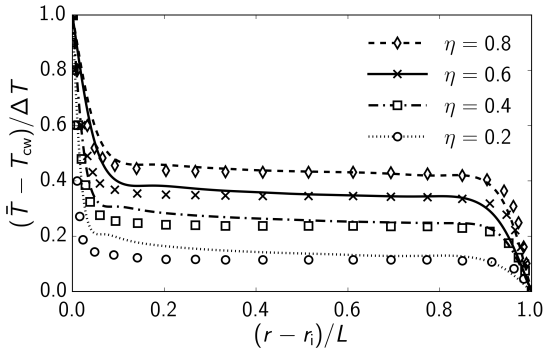

Figure 6. Mean temperature profiles for various radius ratios η and $3 \times 10^6 \leq Ra \leq 10^7$ comparing ODT (lines) with DNS [2] (symbols).

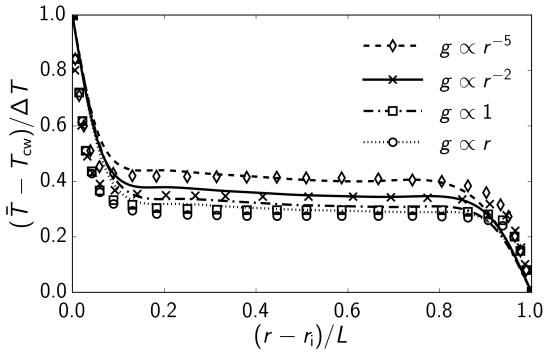

Figure 7. Mean temperature profiles for various gravity profiles $g(r)$ and $7 \times 10^5 \leq Ra \leq 5 \times 10^6$ comparing ODT (lines) with DNS [2] (symbols).

and largest for $g(r) \propto r$. This suggests that the inner and outer thermal boundary layers are more symmetric to each other in the case of a stronger radial decrease of the gravity. The consequence is that, in the case of $g(r) \propto r^{-5}$, the temperature distribution is closer to the planar RB results (see Fig. 3(a)) for which the model parameters C and Z have been obtained. Hence the smaller modelling error.

Looking more carefully at both Figs. 6 and 7 reveals systematically shallower temperature gradients near the confinement walls. This is most prominent at the inner wall, but also present at the outer wall. This is due to conservation of the mean heat flux in stationary statistic under the absence of heat sources within the fluid (no internal heating). The heat transfer (Nusselt number) is thus somewhat underestimated at present by ODT whereas the (thermal) boundary layer thickness is overestimated.

4.2. Asymmetry of the boundary layers

Figs. 6 and 7 exhibit the reduced bulk temperature $T_b < (T_{cw} + T_{hw})/2$ in comparison to the planar case. This implies that the boundary layers at the inner and outer sphere are asymmetric. The asymmetry is captured by ODT for $10^7 \leq Ra \leq 10^{10}$, $0.2 \leq \eta \leq 0.8$, and the four gravity profiles studied.

For $Pr = 1$, the ratio of the outer and inner boundary layer thicknesses is expected to be the same for the thermal and the viscous boundary layer. It can be shown that this ratio depends only on the shell geometry and the background gravity, but not on the Rayleigh number. Boundary layer theory yields [2]

$$\frac{\delta_{T,o}}{\delta_{T,i}} = \frac{\delta_{U,o}}{\delta_{U,i}} = \frac{\chi^{1/6}}{\eta^{1/3}} \quad \text{with} \quad \chi = \frac{g(r_i)}{g(r_o)}. \tag{13}$$

Figures 8(a) and (b) show the ratios of the outer and inner thermal and viscous boundary layer thicknesses for various flow configurations. The thicknesses were obtained with the slope method (cf. Fig. 4). A comparison of ODT results to the theoretical expectation given by Eq. (13) (lines) reveals that the asymmetry of the boundary layers is captured by the ODT model. The modelling error is smaller for the thermal boundary layers. However, the order-of-magnitude of the effect and the trends are correctly predicted by the ODT model for both boundary layers and the values of $\eta > 0.2$ investigated.

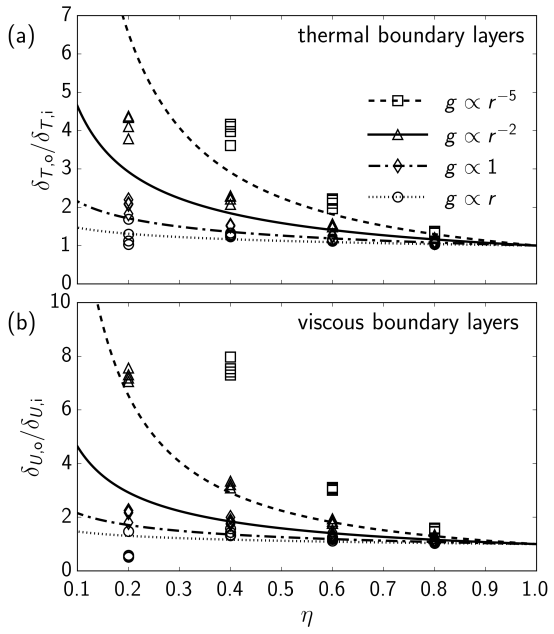

Figure 8. Outer-to-inner ratio of the thermal (a) and viscous boundary layer thicknesses (b) for various radius ratios, gravity profiles, and Rayleigh numbers $10^7 \leq Ra \leq 10^{10}$ at $Pr = 1$.

It is worth to note that there is no systematic Ra-dependency in the results shown in Fig. 8. This suggests that ODT results are in principle consistent with theory. The reference DNS results [2] follow Eq. (13) with notable variance ($\approx 30\%$ for small η) but more closely than the present ODT results. ODT can give similarly robust results as the reference DNS, in particular with respect to the trends, but exhibits also a systematic modelling error.

5. CONCLUSION

Stochastic simulations of turbulent thermal convection have been conducted with an adaptive implementation of the one-dimensional turbulence (ODT) model for planar and spherical geometries [11, 12]. For the present study, the formulation of this model was developed further to account for buoyancy.

There are only two main model parameters in ODT which are related to the flow physics. These parameters need to be determined with the aid of reference data which was done here for an air-filled planar geometry of aspect ratio one and $Ra \sim 10^{10}$ [3, 5]. The optimal parameters were then kept fixed and used to study spherical cell geometry.

It was shown that ODT captures the structure of the thermal and viscous boundary layers over the cooled and heated wall. In spherical geometry, these boundary layers are asymmetric so that the bulk temperature drops. This is captured by ODT even for rather low values of the Rayleigh number ($Ra \lesssim 10^7$). The flow is rather well organised in 3-D for example due to the large-scale circulation [1], plumes [2], and superstructures [6]. All these flow features are not directly resolved in ODT which seems to explain most of the observed differences.

In conclusion, ODT is mainly applicable for turbulent convection at $Ra \gtrsim 10^7$ (with $Pr \simeq 1$). Nevertheless, it could be shown that ODT yields reasonable predictions of flow statistics for a broad ranges of the Rayleigh numbers, gravity profiles, and radius ratios using fixed model parameters. While single-velocity ODT is computationally more efficient, the vector formulation seems to exhibit a higher fidelity.

ACKNOWLEDGEMENTS

MK and HS acknowledge support by the German Academic Exchange Service (DAAD), which is funded by the Federal Ministry of Education and Research (BMBF), Grant no. PPP-USA-2017 (ID-57316240). Part of this work has been conducted within a project funded by the European Regional Development Fund (EFRE), Grant no. StaF 23035000. MK also acknowledges support by a Conference Travel Grant from the Graduate Research School (GRS) of the BTU Cottbus-Senftenberg, Cluster 3, Stochastic Methods for Fluid Flow and Transport Processes.

REFERENCES

[1] Chillà, F., and Schumacher, J., 2012, "New Perspectives in Turbulent Rayleigh–Bénard Convection", *Eur Phys J E*, Vol. 35, 58.

[2] Gastine, T., Wicht, J., and Aurnou, J. M., 2015, "Turbulent Rayleigh–Bénard Convection in Spherical Shells", *J Fluid Mech*, Vol. 778, pp. 721–764.

[3] Ahlers, G., Bodenschatz, E., Funfschilling, D., Grossmann, S., He, X., Lohse, D., Stevens, R. J. A. M., and Verzicco, R., 2012, "Logarithmic Temperature Profiles in Turbulent Rayleigh–Bénard Convection", *Phys Rev Lett*, Vol. 109, 114501.

[4] Zhu, X., Mathai, V., Stevens, R. J. A. M., Verzicco, R., and Lohse, D., 2018, "Transition to the Ultimate Regime in Two-Dimensional Rayleigh–Bénard Convection", *Phys Rev Lett*, Vol. 120, 144502.

[5] Li, L., Shi, N., du Puits, R., Resagk, C., Schumacher, J., and Thess, A., 2012, "Boundary Layer Analysis in Turbulent Rayleigh–Bénard Convection in Air: Experiment versus Simulation", *Phys Rev E*, Vol. 86, 026315.

[6] Pandey, A., Scheel, J. D., and Schumacher, J., 2018, "Turbulent Superstructures in Rayleigh–Bénard Convection", *Nature Comm*, Vol. 9, 2118.

[7] Kerstein, A. R., 1999, "One-Dimensional Turbulence: Model Formulation and Application to Homogeneous Turbulence, Shear Flows, and Buoyant Stratified Flows", *J Fluid Mech*, Vol. 392, pp. 277–334.

[8] Kerstein, A. R., Ashurst, W. T., Wunsch, S., and Nilsen, V., 2001, "One-Dimensional Turbulence: Vector Formulation and Application to Free Shear Flows", *J Fluid Mech*, Vol. 447, pp. 85–109.

[9] Ashurst, W. T., and Kerstein, A. R., 2005, "One-Dimensional Turbulence: Variable Density Formulation and Application to Mixing Layers", *Phys Fluids*, Vol. 17, 025107.

[10] Wunsch, S., and Kerstein, A. R., 2005, "A Stochastic Model for High-Rayleigh-Number Convection", *J Fluid Mech*, Vol. 528, pp. 173–205.

[11] Lignell, D. O., Lansinger, V., Medina, J., Klein, M., Kerstein, A. R., Schmidt, H., Fistler, M., and Oevermann, M., 2018, "One-Dimensional Turbulence Modeling for Cylindrical and Spherical Flows: Model Formulation and Application", *Theor Comp Fluid Dyn*, pp. 1–26, first online 06/12/2018.

[12] Lignell, D. O., Kerstein, A. R., Sun, G., and Monson, E. I., 2013, "Mesh Adaption for Efficient Multiscale Implementation of One-Dimensional Turbulence", *Theor Comp Fluid Dyn*, Vol. 27 (3), pp. 273–295.

[13] Klein, M., and Schmidt, H., 2017, "Stochastic Modeling of Passive Scalar Transport in Turbulent Channel Flows at High Schmidt Numbers", *Proc 10th Int Symp Turb Shear Flow Phen (TSFP10)*, Chicago, IL, Vol. 1, 1B-2.